Reactive and Functional Polymers 221 (2026) 106664

Contents lists available at ScienceDirect

Reactive and Functional Polymers

journal homepage: www.elsevier.com/locate/react

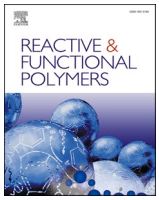

Nanostructure-reinforced epoxy-acrylate interpenetrated networks for UV-curable high-performance coatings

Maksims Jurinovs [a,*], Nikolass Rukavisnikovs [a], Sabine Greivule [a], Olesja Starkova [a], Andrejs Kovalovs [b], Jānis Brunāvs [c], Jan Macutkevič [d], Inna Juhnevica [e], Oskars Platnieks [a], Sergejs Gaidukovs [a,f,*]

[a] Institute of Chemistry and Chemical Technology, Faculty of Natural Sciences and Technology, Riga Technical University, P. Valdena Str. 3, LV-1048 Riga, Latvia
[b] Institute of High-Performance Materials and Structures, Faculty of Civil and Mechanical Engineering, Riga Technical University, Kipsalas Street 6A, LV-1048 Riga, Latvia
[c] Latvian Maritime Academy, Riga Technical University, Kipsalas Street 6A, LV-1048 Riga, Latvia
[d] Institute of Applied Electrodynamics and Telecommunications, Physics faculty, Vilnius University, Sauletekio ave. 3, Vilnius LT-10257, Lithuania
[e] Institute of Physics and Materials Science, Faculty of Natural Sciences and Technology, Riga Technical University, Paula Valdena 3/7, Riga LV-1048, Latvia
[f] Department of Materials Science and Engineering, Korea University, Seoul 02841, Republic of Korea

ARTICLE INFO

Keywords:
Nanofillers
Photopolymerization
UV-curing
Nanoclay
Composite

ABSTRACT

High-performance coatings require rapid and sustainable processing, robust mechanical properties, and long-term durability. However, conventional epoxy systems rely on slow and energy-intensive thermal curing. Here, we develop UV-curable epoxy-acrylate systems optimized through three sequential stages: neat UV-cured epoxy, interpenetrating epoxy-acrylate networks, and nanoclay-reinforced IPN composites. The formulations cure into ~300 μm films under 2 min of UV exposure, removing the need for thermal treatment. The epoxy-acrylate networks exhibit a markedly increased hardness (up to 38% increase) and improved water-barrier performance compared to neat UV-cured epoxy. The incorporation of nanoclay platelets yields nanostructure-reinforced epoxy-acrylate composite coating and further enhances materials' thermal stability, reduces water uptake (by up to 46%), and improves stiffness (by up to 50%). Mechanical property predictions from finite-element analysis (FEA), derived from experimentally measured hardness and modulus values, confirmed the formation of efficiently reinforced and mechanically stable networks across the optimized compositions. Moisture transport was quantified using Fickian sorption models, establishing clear correlations between polymer network architecture, platelet alignment, and material stiffness with water barrier behavior. Together, these results demonstrate a predictable and tunable route to rapidly and sustainably produce high-performance UV-curable epoxy-acrylate coatings for marine environment applications, combining the speed of photopolymerization with the durability of nanoparticle-reinforced thermoset composites.

1. Introduction

High-performance protective coatings play a critical role in extending the lifetime of structural components exposed to chemically aggressive, humid, or mechanically demanding environments. They are widely employed in energy infrastructure, marine systems, transportation, and industrial equipment [1,2]. The increasing industrial shift toward faster manufacturing, higher safety standards, reduced energy consumption, and environmentally sustainable processes has intensified the need for coatings that combine long-term durability with rapid, low-energy curing [3]. Achieving this balance remains one of the central challenges in next-generation coating design.

Epoxy resins represent the benchmark for such applications due to their excellent adhesion, chemical resistance, and inherent thermal and dimensional stability [4]. Their highly crosslinked aromatic networks allow reliable long-term performance in demanding and corrosive environments, making them indispensable in marine, automotive, and aerospace coatings [5]. However, conventional epoxy systems suffer from several intrinsic limitations that restrict their applicability in modern, energy-efficient production lines. Most notably, they require

* Corresponding authors.
E-mail addresses: Maksims.Jurinovs@rtu.lv (M. Jurinovs), Sergejs.Gaidukovs@rtu.lv (S. Gaidukovs).

https://doi.org/10.1016/j.reactfunctpolym.2026.106664
Received 16 December 2025; Received in revised form 21 January 2026; Accepted 24 January 2026
Available online 26 January 2026

prolonged thermal curing, often several hours at temperatures above 100 °C, which increases energy usage, challenges process safety, slows production, and limits the use of heat-sensitive substrates [6]. Additionally, the resulting networks are typically brittle, characterized by low strain-to-failure and susceptibility to cracking under cyclic or impact loading [7]. Together, these factors motivate the development of alternative curing strategies that preserve epoxy performance while overcoming their processing and toughness constraints.

Ultraviolet (UV) curing has emerged as a compelling approach for enabling rapid and energy-efficient polymerization [8]. Photopolymerization enables almost instantaneous crosslinking at room temperature upon exposure to light, enabling coatings to achieve handling or functional strength within seconds to minutes, which is significantly faster than conventional thermal systems [9–11]. The method is inherently solvent-free and substantially reduces manufacturing energy footprints. Despite these advantages, the practical implementation of UV-curable systems remains challenging. Thick films often cure incompletely due to limited light penetration and reduced mobility of radicals. At the same time, surface layers may be inhibited by oxygen [12,13]. Furthermore, for purely acrylate-based networks, prolonged UV exposure can lead to photo-oxidative degradation and discoloration, resulting in a yellowing effect [14]. These issues underscore the need for hybrid UV-curable formulations that offer improved curing depth, reduced sensitivity to oxygen, and enhanced mechanical robustness.

A promising strategy to further overcome limitations of epoxy systems involves the creation of interpenetrating polymer networks (IPNs). IPNs consist of two or more networks polymerized in situ to produce a physically interlocked but not covalently bonded structure [7,15]. This architecture leverages the complementary advantages of different polymer chemistries, i.e., toughness, adhesion, and chemical resistance from epoxies, together with rapid curing and flexibility from acrylates [16,17]. For example, Fan et al. demonstrated that epoxy-acrylate IPNs can significantly improve mechanical strength, damping properties, and resistance to crack propagation [18].

To further enhance mechanical, thermal, and barrier properties, nanoscale fillers such as layered silicates have been widely incorporated into polymer networks [19,20]. Nanoclays, in particular, create tortuous diffusion paths and restrict polymer chain mobility [21,22]. When exfoliated effectively, they can substantially improve modulus, hardness, and hydrophobicity [23–26]. However, their influence on UV curing is complex: depending on dispersion and loading, nanoclays may either accelerate polymerization or hinder it through light scattering and UV absorption [25,27,28].

Prior studies have established two important foundations for UV-curable coatings. First, acrylic-epoxy hybrid/IPN photopolymerizations involve concurrent radical acrylate curing and cationic epoxy ring-opening, leading to hybrid cured films with reduced shrinkage, enhanced toughness, and modified adhesion and damping behavior [29,30]. Second, UV-curable clay nanocomposites, based on either epoxy or acrylate matrices reinforced with organo-montmorillonites, demonstrate that layered silicates can influence cure behavior and thermomechanical response, primarily through nanoscale dispersion and confinement effects [31,32]. Nevertheless, the current literature typically examines either UV-curable epoxies, epoxy-acrylate IPNs, or nanocomposite enhancement in isolation. Little is known about how network architecture, dual-cure kinetics, and filler dispersion jointly evolve in thick UV-cured films, especially under industrially relevant curing times. This limits insight into how network architecture and filler dispersion jointly influence curing, mechanical behavior, and barrier performance of IPN composite systems. Systematic progression from neat UV-curable epoxy to epoxy-acrylate IPNs and finally to nanoclay-reinforced composites within a unified framework remains largely unexplored. In addition, modelling of mechanical characteristics and diffusion-controlled sorption in such hybrid systems is scarce.

In this study we continue our investigation of light-curable high-performance epoxide coatings [33]. In turn, here we address these gaps by developing a unified three-stage UV-curable platform that evolves from (i) neat epoxy, to (ii) epoxy-acrylate IPNs, and finally to (iii) nanoclay-reinforced IPNs. Developed coatings can be fully cured within $\leq$2 min under Hg-lamp UV-irradiation, eliminating the need for thermal post-curing. Through a combination of FTIR monitoring, thermal analysis, DMA, microindentation, finite-element modelling, and diffusion analysis, we establish direct relationships among curing kinetics, network architecture, mechanical reinforcement, and water-barrier performance. This systematic approach demonstrates how formulation design and filler integration can be tuned jointly to achieve rapid, energy-efficient processing while maintaining high mechanical and environmental durability.

2. Experimental section

2.1. Materials

The branched poly(phenyl glycidyl ether)-*co*-formaldehyde (PGEF), kindly supplied by Advanced Polymer Coatings (USA), isobornyl acrylate (IBOA, SARBIO 5102), kindly provided by Arkema, and trimethylolpropane triacrylate (TMPTA), supplied by Sigma Aldrich, were used as the base resins. Quaternary ammonium salt-modified montmorillonite nanoclay (NC, Dellite 67G) was incorporated as a reinforcing filler. Diphenyl(2,4,6-trimethylbenzoyl)phosphine oxide (TPO-L) and triarylsulfonium hexafluoroantimonate (TASHF-Sb) served as radical and cationic photoinitiators, respectively (Sigma Aldrich).

2.2. Sample preparation

PGEF resin was first investigated in its neat form to optimize curing conditions. The resin was mixed with 3 wt% of the cationic photoinitiator TASHF-Sb using magnetic stirring at 750 rpm until a homogeneous solution was obtained. Samples with a controlled thickness of approximately 300 μm were prepared either on glass substrates by using a coating applicator (BYK-Gardner, China) or in silicone molds for sorption and DMA tests. Curing was performed under a 400 W Hg UV lamp with a total surface irradiation intensity of 250 mW cm^{-2} and the irradiation time was systematically varied, as summarized in Table 1, to determine the optimal curing time.

After establishing the irradiation parameters, the concentration of the cationic initiator was optimized. Epoxy resin was mixed with 1, 3, or 5 wt% TASHF-Sb by magnetic stirring, followed by degassing under vacuum. The samples were cast to a thickness of 300 μm and cured under identical UV conditions to identify the most effective initiator content.

The interpenetrating polymer network (IPN) system was then proposed to be developed by introducing acrylates into the epoxy matrix. Epoxy-acrylate weight ratios of 50/50, 70/30, and 90/10 were prepared, with the acrylate fraction consisting of trimethylolpropane triacrylate (TMPTA) and isobornyl acrylate (IBOA) in a fixed 3:1 ratio. The epoxy and acrylates were premixed by magnetic stirring at 750 rpm. Once homogeneous, the optimized amount of TASHF-Sb (relative to the epoxy fraction) and 2 wt% of the radical initiator TPO-L (relative to the acrylate) were added. The mixtures were degassed under vacuum and cast into ~300 μm thick coatings on glass, which were subsequently cured under the same Hg lamp for 90 s.

Finally, nanocomposites were prepared using the optimized IPN formulation as the matrix. Quaternary ammonium salt modified nanoclay was incorporated at 0.5, 1, 3, and 5 wt% relative to the total epoxy-acrylate mass. To achieve uniform dispersion, the formulations were processed by ultrasonication for 30 min, with intermittent pauses to prevent overheating, while simultaneously stirred magnetically at 750 rpm. After cooling to room temperature, the optimized amounts of TASHF-Sb and TPO-L were added, and the mixtures were further

Table 1
Prepared compositions in optimization order (*bold for optimal formulation*).

Sample name***	Epoxy (wt%)	IBOA (wt%)	TMPTA (wt%)	TASHF-Sb (wt%)*	TPO-L (wt%)**	Nanoclay (wt%)	UV curing (s)
Optimization of curing time with set initiator content							
	100	–	–	3	–	–	30
	100	–	–	3	–	–	60
E_3wt	**100**	**–**	**–**	**3**	**–**	**–**	**90**
	100	–	–	3	–	–	120
	100	–	–	3	–	–	150
	100	–	–	3	–	–	300
Optimization of initiator content							
	100	–	–	1	–	–	30
E_1wt	100	–	–	1	–	–	60
	100	–	–	1	–	–	90
	100	–	–	5	–	–	30
E_5wt	100	–	–	5	–	–	60
	100	**–**	**–**	**5**	**–**	**–**	**90**
Optimization of UV-curable IPN							
E50A/50	50	12.5	37.5	5	2	–	90
E70/A30	70	7.5	22.5	5	2	–	90
E90/A10	**90**	**2.5**	**7.5**	**5**	**2**	**–**	**90**
Optimization of nanoclay concentration in acrylate/epoxy IPN							
0.5wt_NC	90	2.5	7.5	5	2	0.5	90
1wt_NC	90	2.5	7.5	5	2	1	90
3wt_NC	90	2.5	7.5	5	2	3	90
5wt_NC	90	2.5	7.5	5	2	5	90

* TASHF-Sb (wt%) is calculated based on epoxy mass.
** TPO-L (wt%) is calculated based on total acrylate mass.
*** Bold indicates chosen formulation for further tests.

homogenized by high-shear mixing at 7000 rpm for 90 s. The prepared dispersions were degassed under vacuum and cured as ~300 μm thick films under a 400 W Hg UV lamp (250 mW cm^{-2}) for 90 s. The coating thickness was selected to meet high-durability performance requirements, as dry film thicknesses in the range of 250–350 μm are commonly specified for heavy-duty protective coatings (as per ISO 12944 standard).

2.3. Fourier transform infrared (FTIR) spectroscopy

The interactions between the printed samples and raw resins were examined using an FTIR spectrometer (Nicolet 6700, Thermo Scientific, Germany). On a diamond crystal, a droplet of the resin or a piece of UV-cured sample was placed and secured with a torque wrench using constant pressure. The spectrum was obtained as an average of sixteen separate spectra recorded in the 400–4000 cm^{-1} range with a resolution of 4 cm^{-1}.

2.4. Colorimetry measurement

Color change was measured using a sphere spectrophotometer (Ci7600, X-Rite Pantone, Michigan, USA). For each specimen, three replicate measurements were performed using the total-transmittance port (6 mm aperture) over the spectral range of 360–750 nm with a photometric resolution of 0.01%. During measurements, a white backing was placed behind the samples to minimize background show-through. Color differences were calculated using the manufacturer's software, with the 30 s UV-cured sample used as the reference.

2.5. X-ray diffraction (XRD) measurement

The crystalline phases of E_5wt, E90/A10, NC_0.5wt, NC_1wt, and NC_3wt were analyzed using a Rigaku Ultima + X-ray diffractometer (Rigaku Corporation, Tokyo, Japan) equipped with Cu Kα radiation source (λ = 1.54059 Å) operating at 40 kV and 20 mA. Diffraction patterns were collected over a 2θ range of 5.0°-60.0°, with a goniometer speed of 2°/min. Phase identification for all samples was performed by comparing the obtained diffractograms with reference patterns from the ICDD PDF 5 + 2025 database.

2.6. Dynamic mechanical analysis

Dynamic mechanical analysis (DMA) was executed in a tension mode using a DMA/SDTA861e (Mettler Toledo). All samples had an identical size (8.50 × 4.20 × 0.30 mm). The experiment utilized a temperature range of −20 to +200 °C, an applied force of 5 N, an elongation of 10 μm, a frequency of 1 Hz, and a heating rate of 3 °C min^{-1}.

Temperature dependences of the storage modulus E' were described by the Guo model: [34].

$$E'(T) = E'_g - \frac{E'_g - E'_r}{e^{-k\bullet(T-T_g)} + 1} \quad (1)$$

where E'_g and E'_r are the storage moduli in the glassy and rubbery regions, respectively. The parameter k characterizes the steepness (or breadth) of the transition region and reflects the intrinsic rate of increase in the number of rubbery-state molecular segments with temperature; a smaller k value corresponds to a broader transition. The parameter T_g in Eq. (1) represents the temperature at which the storage modulus decreases most rapidly, i.e., the glass transition temperature. Although it does not necessarily match the T_g value determined from the tan δ peak.

To investigate the effect of NC concentration on the elastic properties of the coatings, conventional micromechanical models were employed. As a first approximation, the rule of mixtures was applied:

$$E = E_m(1 - V_f) + E_f V_f \quad (2)$$

Where E_m and E_f are the elastic moduli of the polymer matrix and the filler, respectively, and V_f is the filler volume fraction. E_m corresponds to the modulus of the neat 90/10 system, and the elastic modulus of NC nanoplatelets was taken as E_f = 175 GPa [35].

The MMT volume fraction in the nanocomposites was calculated using [36]:

$$V_f = \frac{w_f \rho_m}{w_f \rho_m + (1 - w_f)\rho_f} \quad (3)$$

where w_f is the NC weight fraction in the composite, ρ_m and ρ_f are the

densities of the polymer matrix and the filler, respectively. In this study, $\rho_f = 1.7$ g cm^{-3} (as specified in the datasheet), and $\rho_m = 1.29$ g cm^{-3} (as measured experimentally, Table S2).

The next model used is the Halpin-Tsai model, which accounts for the geometry and orientation of the filler particles. The elastic modulus of composites containing exfoliated NC fillers primarily oriented along the loading direction can be expressed as [37]:

$$E = E_m\left(\frac{1+\xi\eta V_f}{1-\eta V_f}\right) \text{ where } \eta = \frac{E_f/E_m - 1}{E_f/E_m + \xi} \quad (4)$$

Here ξ is a shape factor that depends on the geometry and aspect ratio of the filler. For platelet-like fillers, it is defined as $\xi = 2L/W$, where L and W are the length and width of the filler particles, respectively. According to the nanoclay supplier's datasheet, an aspect ratio of $L/W = 200$ was used. In the present analysis, the experimental values of the elastic modulus were taken as the storage modulus measured at 25 °C.

2.7. Microhardness

All microhardness measurements were performed with a Vickers-type indenter (M-171021). Tests were performed on a ~ 300 μm thick coating on glass. Using a hydraulic press with a load of 0.05 kg and 4× magnification, with a dwell time of 20 s. All tests were performed at 21 ± 1 °C. At least 12 indentations were made at randomly chosen locations. Then the average diameter was determined using the data obtained from d_1 and d_2, and was determined using:

$$HV = 0.189\frac{F}{d^2} \quad (5)$$

where F – the indentation force, N; d – average length of the two diagonals after indentation, mm.

2.8. Indentation modelling

Knowing the depth of penetration can help solve the inverse problem for identifying the mechanical properties of research materials. Identification involves numerical experimental methods, which are based on experimental design and approximation techniques. The indenter was imprinted to the prescribed depth under varying elastic property conditions of the test material. The indentation forces predicted through numerical simulations were systematically compared with experimental measurements to reduce discrepancies and achieve closer agreement between the simulated and observed mechanical responses.

Using Vickers' hardness value d can be calculated as:

$$d = \sqrt{0.189\ \frac{F}{HV}} \quad (6)$$

Knowing the diagonal of the indenters imprint, the depth of its penetration can be determined from the following equation:

$$h = \frac{F}{2\ tan\ \frac{136^\circ}{2}} \quad (7)$$

Finite Element analysis (FEA) of the indentation process was conducted in ANSYS Mechanical to reproduce the experimental load-displacement behavior and determine the Yield Strength. A 3D quarter-symmetry FE model was built using SOLID185 elements. The indenter-sample interaction was modelled with CONTA174 and TARGE170 contact pairs, assuming a friction coefficient of 0.15. The indenter material was assigned diamond properties (E = 1140 GPa, Poisson's ratio is 0.07), and the sample was modelled with a constant Poisson's ratio of 0.2. The indentation process was simulated in two stages – loading (penetration) and unloading (elastic recovery), using a bilinear stress-strain material model. A 3^3 Full Factorial Design (FFD) approach was applied to calculate indentation forces for different combinations of Young's Modulus (YM) and Yield Strength (YS) corresponding to the various nanoclay contents. These results were later used to construct regression equations for identifying mechanical parameters.

2.9. Sessile drop

Sessile drop measurements were performed on a Theta Lite optical tensiometer (Attension, China) at room temperature (21 ± 1 °C) using cured coating specimens with a thickness of 300 μm. A deionized water droplet was deposited on the surface, and its profile was recorded in real time for 30 s using a contact angle goniometer equipped with live analysis software. For each sample, at least ten individual measurements were carried out at different surface locations. Contact angle values were extracted at 5 s, 20 s, and the mean value over the 30 s measurement interval was calculated. These three values ("5 s," "20 s," and "average after 30 s") were averaged across all replicates and reported as mean ± standard deviation.

2.10. Density

Density was determined using a density measurement apparatus (Sartorius YDK 01, Germany). The density of ethanol was first verified using a hydrometer. Each sample was weighed in air on the upper pan, then transferred to the lower pan and fully immersed in ethanol to obtain the apparent weight in liquid. Sample density was calculated according to Archimedes' principle from the measured air and immersion weights.

2.11. Water absorption

All samples were selected with nearly identical surface areas and weights (18.00 × 4 × 0.3 mm), ensuring that the final results would not be dependent on sample size. Every sample was fully submerged in distilled water and left for a particular time at room temperature (21 ± 1 °C). Then, every sample was tapped dry one by one with tissue and immediately scaled. At least 3 parallel measurements were done for each sample.

The experimental water-absorption data were fitted using the 1D Fickian diffusion model, expressed as [38,39]:

$$\frac{M(t)-M_0}{M_\infty - M_0} = 1 - \frac{2}{\pi^2}\sum_{k=1}^{\infty}\frac{\left[1-(-1)^k\right]^2}{k^2}\exp\left(-\left(\frac{\pi k}{a}\right)^2 Dt\right) \quad (8)$$

Where M_∞ is the equilibrium (saturation) water content, D is the apparent diffusion coefficient, and a is the sample thickness. The initial water content M_0 was assumed to be zero.

To analyze the dependence of diffusivity on the NC content in the composite coatings, the Nielsen model was applied [40]:

$$D = \frac{D_m}{1+(L/2W)V_f} \quad (9)$$

where D_m is the diffusivity of the neat system (in this study, $D_m = 0.6 \cdot 10^{-3}$ mm^2/h, as determined experimentally), V_f is defined by Eq. (3), and $L/W = 200$ was used as in Eq. (4).

3. Results and discussions

3.1. Macromolecular network formation and thermal properties

The proposed optimisation strategy for developing the UV-curable epoxy-acrylate interpenetrating network (IPN) system is shown in Scheme 1. First, the optimal UV exposure window is identified, defined as the point where the epoxy network reaches maximum hardness and thermal stability without entering over-curing. This optimized epoxy

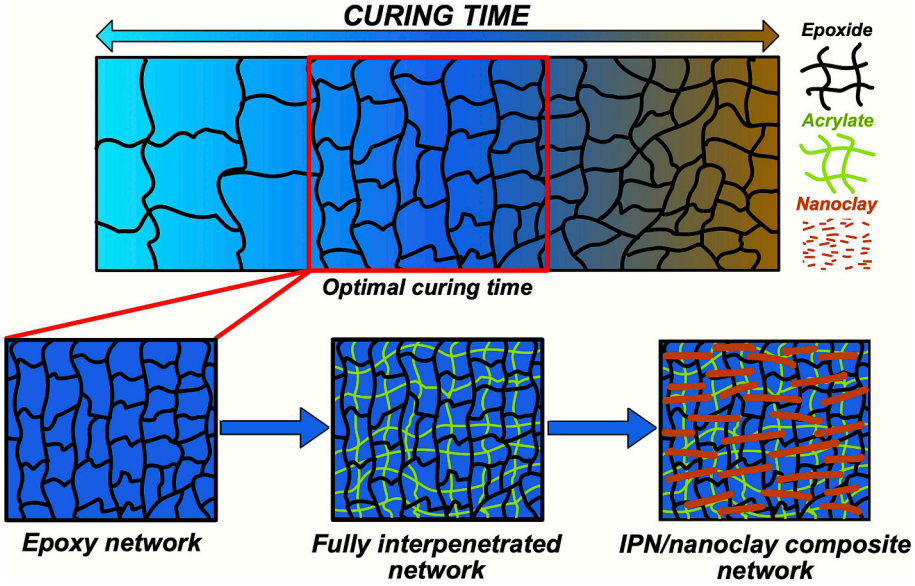

Scheme 1. Schematic representation of the three-step optimisation strategy for developing high-performance UV-curable epoxy-acrylate IPN composite coating.

baseline then supports the formation of a dense IPN upon the addition of acrylate monomers, which improves both mechanical strength and barrier performance. The schematic representation of the macromolecular chain networks formed during epoxide cationic polymerization and acrylate radical polymerization is shown in Scheme S1. In the final step, exfoliated nanoclay (NC) platelets are incorporated into the macromolecular network to create a reinforced interphase that restricts segmental mobility and increases load transfer efficiency. This three-stage approach, which combines curing optimization, network design, and nanoscale reinforcement, provides a scalable route for producing fast-curing, high-performance coatings suitable for demanding industrial environments.

The mechanism of cationic photopolymerization, involving in situ Brønsted acid formation and subsequent epoxide ring opening chemical reactions, is well described in the literature and schematically shown in supplementary Scheme S1a [41,42]. Epoxy photopolymerization conditions were investigated by varying UV exposure time (30–300 s for 3 wt% and up to 90 s for 1 and 5 wt%) and photoinitiator (PI) concentration (1, 3, and 5 wt%), as characterized by FTIR spectra (Fig. 1a, S1, S2, S3). The spectra confirmed efficient UV absorption and epoxy ring opening after 30 s (Fig. S1) and at PI contents of at least 3 wt% (Fig. 1a), as evidenced by the disappearance of the epoxy band at 907 cm^{-1}. Prolonged irradiation, however, induced (tested for 3 wt% PI) a clearly visible yellowing of the films and detachment from the substrate for curing times exceeding 150 s (Fig. S4). Colorimetric analysis (Table S1) shows increasing discoloration with prolonged UV exposure. Relative to the 30 s irradiated sample as reference, Δb values remain low at 60–90 s (≤3.26), indicating negligible to marginal yellowing, but increase sharply at ≥120 s, reaching severe yellowing at longer exposure times. Simultaneously, Δa shifts from negative to strongly positive values, indicating a transition from yellowing to brownish discoloration, while increasingly negative ΔL reflects progressively darker coatings. Such discoloration is a characteristic sign of photo-degradation, caused by chemical changes in the polymer's molecular structure [14]. During this process, UV irradiation generates free radicals through bond cleavage and hydrogen abstraction within the polymer backbone. These radicals subsequently react with oxygen to form unstable radical moieties, which promote polymer chain scission and the formation of oxidized species, including carbonyl-containing fragments. [43]. This transformation is clearly evident in the FTIR spectra (Fig. S1): both the carbonyl C═O absorption band at 1724 cm^{-1} and the broad hydroxyl -OH band around 3400 cm^{-1} increase with prolonged UV exposure [44–46]. It should be noted that the OH band partially originates from the resin itself, as indicated by the dotted reference spectrum. The formation of carbonyl groups also introduces chromophores, which absorb UV and parts of the visible light by exciting electrons from their ground state to an excited state, leading to discoloration (yellowing or darkening) [43].

The incorporation of IBOA/TMPTA acrylate into the epoxy resin, resulting in an interpenetrated network (IPN), is evident in the FTIR spectra. Characteristic absorbance bands, including the distinct vinyl C—H out-of-plane vibration band at 810 cm^{-1} and carbonyl C═O stretching vibration band at 1733 cm^{-1}, appear and increase in intensity with increasing acrylate content (Fig. 1b). During UV exposure, both the epoxy (907 cm^{-1}) and vinyl (810 cm^{-1}) bands progressively decrease, demonstrating the development of an interpenetrating dual-network IPN structure. Importantly, no additional peaks appear in the spectra confirming efficient polymerization. Quantitative FTIR conversion analysis could not be performed due to spectral overlap and the lack of a stable reference band [47]. The acrylate C═C region (1630–1640 cm^{-1}) cannot be reliably resolved because it overlaps with aromatic vibrations from the PGEF epoxy, while the 810 cm^{-1} band cannot be reliably deconvoluted after curing. Although the epoxy oxirane band (900–920 cm^{-1}) is observable, concurrent changes in aromatic and ether-related bands during IPN formation prevent reliable normalization.

For the IPN/NC composites (Fig. 1c), the epoxy band at 907 cm^{-1} remains primarily consumed after UV curing at lower NC loadings (0.5–1 wt%). Still, it remains more intense at higher NC loadings (>3 wt %), indicating partial inhibition of epoxy ring opening. In contrast, the acrylate band at 810 cm^{-1} largely disappears for all formulations after curing, leaving only a slight shoulder. The influence of NC on UV polymerization remains a topic of debate in the literature. Several studies report a reduced polymerization rate, regardless of the clay type, due to the light absorbance of NC, which arises from light scattering by the clusters [48,49]. Conversely, Datta et al. demonstrated that the addition of 2 wt% NC significantly increased the acrylate polymerization rate, achieving a 77% conversion in 5.5 h, in contrast to the sample without NC, which reached only a 58% conversion [50]. At the same time, Peila et al. reported that 5 wt% NC in the UV-curable systems did not affect the curing rate, attributing this to scattering phenomena from silicate platelets that interfered with the UV light [51]. Using RT-FTIR and photo-DSC, Landry et al. demonstrated that the influence of clay on UV polymerization rate and acrylate conversion depends not only on the clay loading but also on the quality of the dispersion and formulations' viscosity increase, noting that 1 wt% well-dispersed NC did not

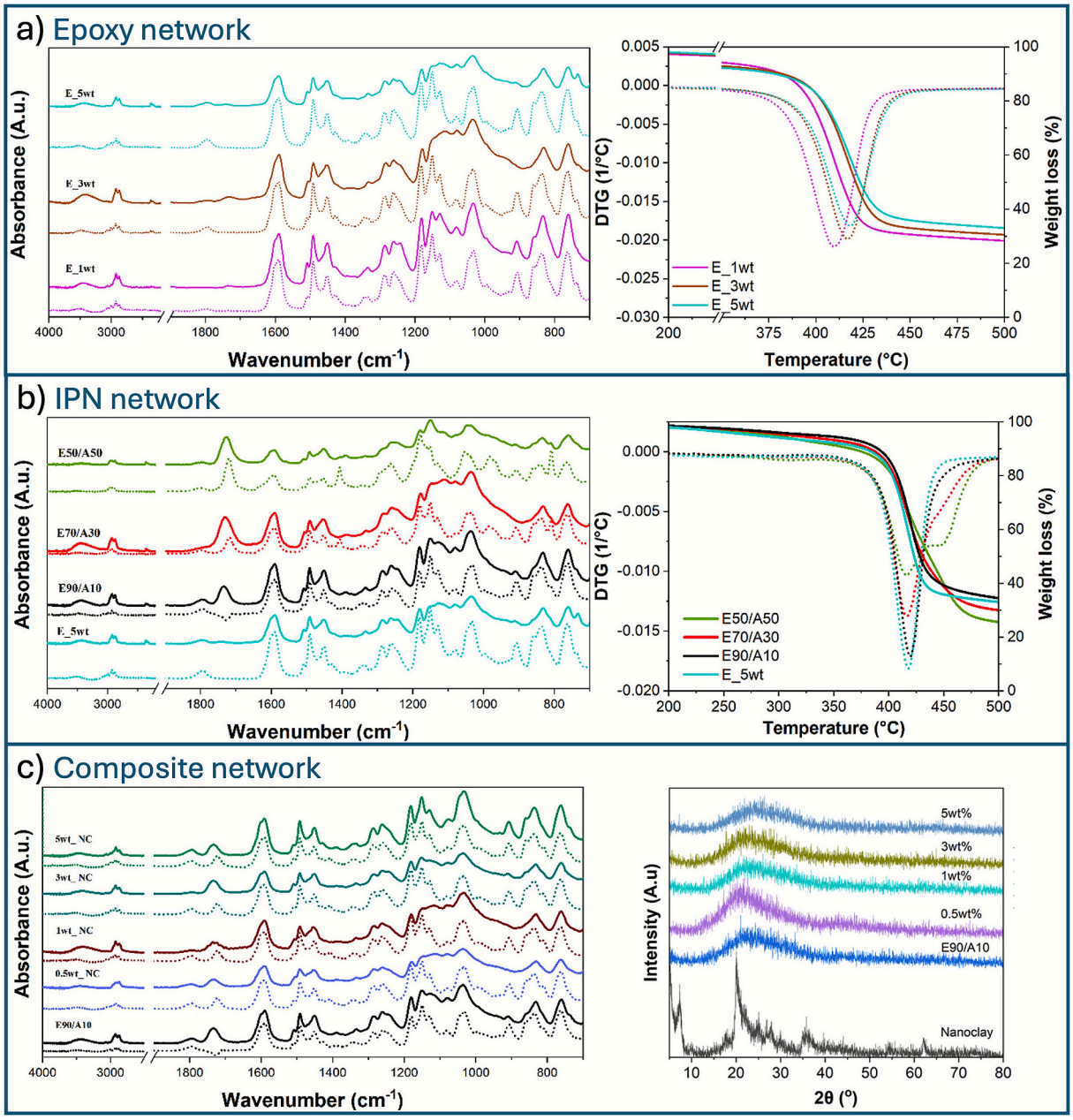

Fig. 1. (a) FTIR spectra before (dotted lines) and after (solid lines) UV-curing (left) and TGA curves of UV-cured samples with different PI loadings at 90 s curing time (right); (b) FTIR spectra before (dotted lines) and after (solid lines) UV-curing (left) and TGA curves of UV-cured samples with different acrylate loadings at 90 s curing time (right); (c) FTIR spectra before (dotted lines) and after (solid lines) UV-curing (left) and XRD spectra of epoxy-acrylate IPN composite with different NC loadings (right).

significantly impede UV penetration [51].

Fig. 1c shows the XRD patterns of pristine montmorillonite NC and UV-cured epoxy/nanoclay nanocomposites. The pristine NC exhibits a distinct diffraction peak at approximately $2\theta \approx 6.5°$, corresponding to the [001] basal reflection with an interlayer spacing (d_{001}) of about 1.36 nm, confirming its well-ordered lamellar structure. In contrast, all nanocomposite samples display the disappearance of this peak, leaving only a broad amorphous halo centered near 20°, which originates from the epoxy matrix. The absence of the [001] reflection indicates a complete loss of long-range order of clay platelets. This suggests extensive exfoliation or disordered state of NC platelets within the polymer network. While XRD alone cannot fully distinguish complete exfoliation, the absence of any shifted basal reflections suggests that ordered intercalated structures are not present. When considered together with the observed improvements in mechanical performance, discussed further, and thermal stability, these results are consistent with effective dispersion of NC platelets within the epoxy network during UV curing [52,53].

Thermogravimetric analysis (TGA) and its respective derivative (DTG) curves of the UV-cured PGEF epoxy systems, as shown in Fig. 1a, S5-S7, indicate a single dominant degradation stage occurring between 375 and 450 °C, typical of aromatic epoxy networks [54]. For 3 wt% PI (Fig. S5), increasing UV exposure time from 30 s to 120 s produces a gradual shift of mass loss curves and the maximum degradation temperature (T_{max}) toward higher temperatures, from 412 to 422 °C. This indicates an increase in crosslink density within the epoxy network resulting from prolonged UV curing. As curing proceeds, the amount of unreacted epoxy groups decreases, and a tightly crosslinked structure enhances the overall thermal stability. At extended exposure times of >150 s, both mass loss curves and T_{max} shift slightly to lower temperatures, and the DTG peak indicates a reduction of T_{max} and peak width.

These changes align with the visual browning of the films and FTIR-detected increases in carbonyl and hydroxyl absorption bands, indicative of UV-induced photo-oxidative degradation. Prolonged exposure likely promotes local chain scission and oxidation of aromatic and ether linkages, generating thermally labile sites that initiate decomposition at lower temperatures [55]. The char yield at 500 °C remains nearly constant up to 120 s, reflecting the formation of a highly aromatic, densely cross-linked network; however, it increases noticeably after 150 s. This higher residual mass likely originates from carbonization of over-cured, highly crosslinked domains formed during excessive UV exposure.

The effect of PI concentration on thermal stability is shown in Fig. 1a. Formulations containing 1, 3, and 5 wt% PI all exhibit a single dominant degradation stage spanning ~350–450 °C. Increasing PI content systematically shifts T_{max} from 409 °C (E_1wt) to 418 °C (E_5wt), while simultaneously reducing DTG peak intensity. These trends indicate more efficient network formation and higher crosslink density. The 1 wt% PI formulation exhibits an earlier decomposition onset at approximately 350 °C and a sharper DTG peak, consistent with incomplete cure and the presence of residual epoxy groups. In contrast, the 5 wt% PI sample exhibits the highest T_{max} and the highest char yield, indicating a more fully developed network with superior thermal resistance.

The thermal behavior of the epoxy-acrylate IPNs (Fig. 1b) further illustrates how the compositional balance shapes the degradation mechanism. Although all samples initiate their central mass-loss region near 350 °C, the introduction of acrylates modifies both the degradation temperature and the degradation pathway. The neat epoxy (E_5wt) shows a single peak centered at 418 °C. Incorporating 10 wt% acrylate slightly shifts the degradation region to higher temperatures, whereas the 70/30 and 50/50 systems show a modest reverse shift. Concurrently, the primary DTG peak (~421 °C) decreases in intensity, and a secondary shoulder emerges near 450 °C. This is attributed to the decomposition of acrylate-rich regions, which are typically more crosslinked and therefore thermally more stable [56]. Despite a slight upward shift in the onset of degradation for low acrylate loadings, the char yield systematically decreases with increasing acrylate fraction. Such a decrease reflects the reduced aromatic content and the higher volatility of aliphatic segments. The transition from a single-step to a two-step degradation profile confirms the presence of distinct epoxy- and acrylate-dominated degradation pathways. The sole exception is the E90/A10 formulation, which shifts to higher T_{max} (422 °C) and shows a comparatively higher char yield (~37%). This behavior suggests a more compact and efficiently crosslinked IPN network, where small acrylate domains act as reinforcing bridges within the epoxy matrix. Such structural densification can enhance mechanical rigidity, dimensional stability, and moisture-barrier performance by reducing segmental mobility and restricting diffusion pathways [17,30,57].

Incorporation of NC into the IPN matrix did not produce substantial changes in the thermal stability of the already thermally robust network (Fig. S7). At NC loadings up to 1 wt%, only marginal improvements are observed: the char yield increases by ~1–2%, and T_{max} shifts slightly from 420 °C to 423 °C. However, higher NC contents (3 and 5 wt%) shift the mass-loss curves to lower temperatures, with corresponding decreases in T_{max} to 417 °C and 415 °C, respectively. This reduction in thermal stability is consistent with the previously noted under-curing at elevated clay loadings. ~~Where~~ Reduced UV penetration and reduced epoxy conversion lead to networks with lower crosslink density. Such loosely crosslinked structures contain a greater fraction of thermally labile segments, accelerating the onset of degradation.

3.2. Thermomechanical properties of developed coatings

Dynamic mechanical analysis (DMA) allowed for the evaluation of the temperature-dependent mechanical response of the networks. After the glass transition, increased segmental mobility leads to softening in the rubbery state; therefore, compositions with higher T_g values are preferable for coatings operating across wider temperature ranges. The formation of the crosslinked network was found to be highly dependent on the curing parameters. As shown in Fig. S9, the storage modulus (E′) curves exhibit a progressive shift of the modulus drop (glass transition region) toward higher temperatures with longer curing times. For the 30-s-cured 3 wt% PI sample, the initial decrease in E′ begins near 20 °C, whereas for longer curing times, the onset occurs around 35 °C. The plateau region shifts to higher temperatures of approximately 60, 90, 140, and 150 °C for curing times of 30, 60, 90, and 120 s, respectively. The tan δ curves (Fig. S9) display broad, multi-step transitions, reflecting the heterogeneous crosslinking of the branched polymer network. Regions of higher and lower crosslink density result in local T_g variations and a distribution of relaxation times. The onset of glass transition shifts from below 10 °C for the 30 s sample to 30–40 °C for the 90 s and 120 s samples, while the main T_g peak increases by approximately 70 °C above 60 s curing. The observed yellowing in samples cured for longer than 90 s aligns with the DMA data, confirming that no significant improvement occurs beyond this point.

In the next stage, the effect of PI concentration was examined. The storage modulus and tan δ (Fig. 2a) curves exhibited similar trends to those observed for varying curing times. At 1 wt% PI, a sharp decrease in E′ and a narrow glass transition region were observed, which are undesirable for durable coating applications. Increasing the PI content to 3 wt% and 5 wt% resulted in enhanced performance, with the 5 wt% formulation exhibiting a delayed onset of modulus drop at approximately 55 °C, approximately 20 °C higher than the 3 wt% sample. The tan δ peak for the 5 wt% formulation was narrower and shifted to a higher temperature, indicating a more homogeneous and efficiently crosslinked network.

Next, the effect of acrylate incorporation and interpenetrating network (IPN) formation on the thermo-mechanical behavior was investigated. As shown in Fig. 2b, all epoxy-acrylate compositions exhibit similar storage modulus profiles, characterized by a high-modulus glassy region and a sharp decline near the glass-transition region. However, the tan δ responses (Fig. 2b) reveal a pronounced dependence on acrylate content. The onset of the glass transition for E_5wt% and E90/A10 systems occurs approximately 12–15 °C higher than that of E70/A30 and E50/A50, indicating a gradual reduction in network rigidity with increasing acrylate fraction. The broader and more intense tan δ peaks observed for the high-acrylate formulations suggest increased molecular mobility and enhanced viscous damping associated with a less tightly crosslinked network. This behavior reflects the transition from a predominantly epoxy-rich continuous phase to a more co-continuous IPN structure, where flexible acrylate segments plasticize the epoxy network and facilitate cooperative segmental motion [58]. The narrowing of the tan δ peak for low-acrylate systems further supports a higher degree of inter-network coupling and more uniform crosslink distribution. In contrast, at higher acrylate contents, partial phase separation and reduced interpenetration efficiency can lead to heterogeneous relaxation. These results demonstrate that limited acrylate incorporation ($\leq$ 10 wt%) enhances the rigidity and thermal stability of the IPN by introducing additional crosslink points and interfacial coupling. In contrast, higher acrylate contents increase flexibility but lower the effective glass-transition temperature and modulus.

Finally, the effect of NC incorporation was investigated for loadings ranging from 0.5 to 3 wt%. The incorporation of NC platelets up to 1 wt % restricts segmental mobility within the IPN, as reflected in the increased glassy and rubbery storage moduli compared to the neat polymer (Fig. 2c, Table 2). For instance, E'_g increases by ~60%, E'_r by ~50%, indicating effective polymer-filler interactions and enhanced network constraint. Although T_g decreases from ~133 °C for the neat IPN to 118–115 °C for the 0.5–1 wt% NC composites, the characteristic shoulder drops in storage modulus associated with the relaxation of acrylate-rich and epoxy-rich domains occur at similar or slightly higher temperatures in the nanocomposites. For example, the second relaxation shoulder appears at ~95 °C in the neat IPN and shifts to ~100 °C in NC-filled samples, indicating that domains in proximity to well-dispersed

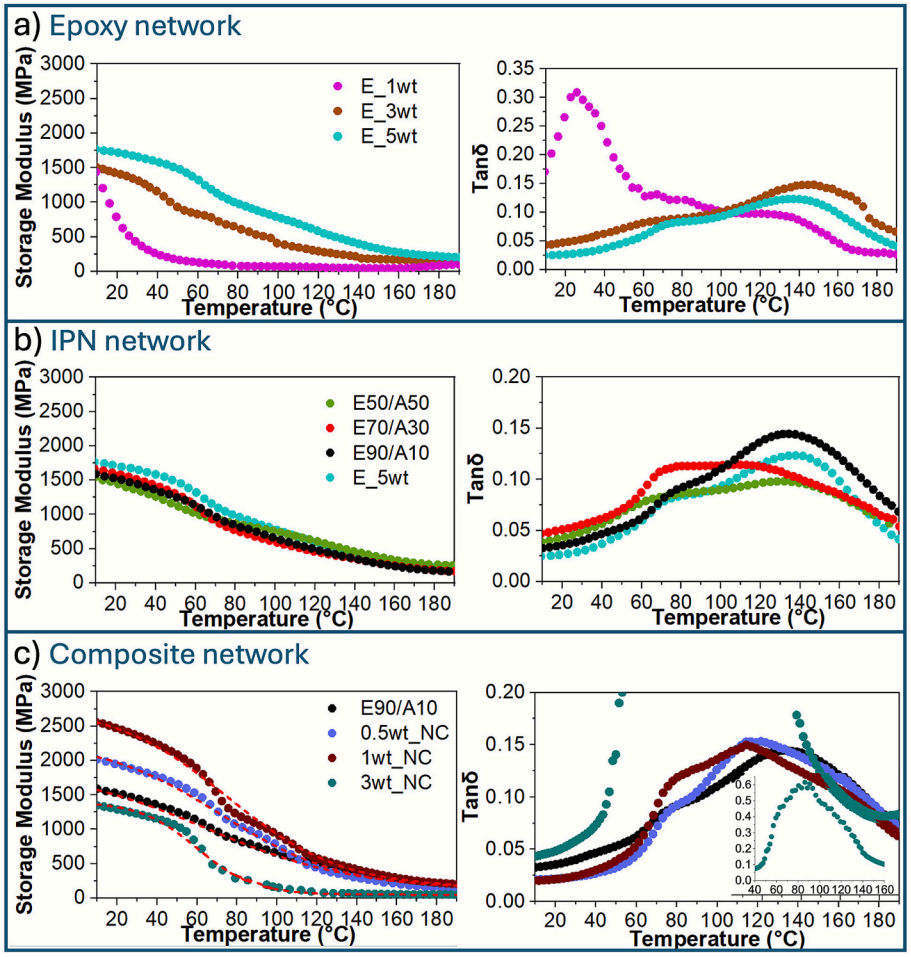

Fig. 2. Storage modulus (E′, left) and tan δ (right) for (a) epoxy samples with different PI contents cured for 90 s, (b) for epoxy-acrylate IPNs with varying component ratios, (c) epoxy-acrylate IPNs with different NC loadings. Dashed (red) lines represent approximations by Guo's model Eq. (1). (For interpretation of the references to color in this figure legend, the reader is referred to the web version of this article.)

Table 2
DMA characteristics and parameters of the Guo model of nanocomposites.

Sample	Experimental				Guo model			
	E'_g, MPa (25 °C)	E'_r, MPa (190 °C)	T_g, °C (tan δ peak)	tan δ	E'_g, MPa	E'_r, MPa	T_g, °C	k
E90/A10	1486	133	133	0.145	1900	120	65	0.027
0.5wt_NC	1906	163	118	0.154	2300	130	72	0.033
1wt_NC	2414	204	115	0.151	2800	150	75	0.035
3wt_NC	1254	51	86	0.616	1400	50	60	0.07

NC platelets exhibit increased local stiffness and more restricted segmental motion. The downward shift of the tan δ peak reflects the redistribution of relaxation spectra: mobile domains dominate the loss response, while stiffened interphase regions relax at higher temperatures. At the highest loading (3 wt%), the crosslinked IPN structure was noticeably disrupted, as evidenced by the pronounced decrease in storage modulus (Fig. 2c) and the substantial increase in the tan δ peak, indicating a transition toward a softer, highly viscoelastic, and only partially cured material.

The temperature dependence of the storage modulus was analyzed using the Guo model Eq. (1), which provides a statistical-mechanical description of how rubbery-state chain segments develop across the glassy-to-rubbery transition [34]. The Guo-model parameters are summarized in Table 2. The values of model parameters E'_g and E'_r follow the same trend, increasing with the increase in NC content. The model-predicted T_g rises by ~10 °C at 1 wt% NC, also indicating effective polymer-filler interactions and enhanced network constraint within the IPN. The parameter *k*, describing the steepness of the glass transition region, increases by ~30% at 1 wt% NC, consistent with a sharper transition associated with reduced chain mobility in filler-interacting segments. The nanocomposite containing 3 wt% NC deviates from this general trend: E'_g, E'_r, and T_g are markedly lower than those of the neat polymer due to chain plastification through aliphatic chains from organically modified NC [59]. This leads to, steric hindrance and UV-blocking by the clay platelets, lowering the curing efficiency, increasing the fraction of unreacted groups and yielding a less cross-linked network. At the same time, the glass-to-rubbery transition becomes significantly steeper, with the *k* parameter nearly twice that of the 1 wt% NC sample. This behavior likely results from incomplete curing as discussed before.

To further evaluate the reinforcing efficiency of NC in the epoxy-acrylate IPN system, the E'_g were analyzed as a function of filler content using well-established micromechanical models. The most straightforward approach is the rule of mixtures Eq. (2), which assumes that all exfoliated NC platelets are perfectly aligned in the loading direction [35]. As seen from Fig. 3, the rule of mixtures noticeably overpredicts the experimental values. To achieve a more accurate description, the Halpin-Tsai model for E_1 Eq. (4) was applied. This model considers the geometry, aspect ratio, and orientation of the filler particles, resulting in a more accurate prediction of the composite modulus for systems containing plate-like nanofillers, such as NC [35].

The Halpin-Tsai model for platelets oriented in the loading direction reproduces the experimental data with remarkable accuracy (Fig. 3), supporting the hypothesis of extensive NC exfoliation and favorable nanoplatelet orientation [35]. The 3 wt% NC sample strongly deviates from the overall trend, as discussed above, and is ineffective as a reinforcing system due to incomplete curing from the UV-blocking effect by NC agglomerates [59].

3.3. Hardness and FEA modelling of developed coatings

To understand how UV exposure and PI concentration govern the development of the epoxy network, the curing behavior was followed through Vickers microhardness (HV) and pencil hardness measurements. Both parameters reflect the evolving crosslink density during photopolymerization, making them highly sensitive indicators of when the network reaches complete cure and when excessive irradiation begins to deteriorate the coating [60]. As shown in Fig. 4a, hardness in the 3 wt% PI formulation rises quickly: HV increases from 87 MPa at 30 s to more than 230 MPa at 60 s, reaching roughly 257 MPa at 90 s. This steep increase captures the rapid establishment of the epoxy network under UV light.

However, extending exposure to 120 s causes HV to drop to 239 MPa, signalling the onset of embrittlement and surface degradation. At even longer exposures, the coatings exhibited pronounced cracking and eventually detached from the substrate, indicating that prolonged UV irradiation starts to damage the chemically fragile sites within the forming network. A similar tendency is observed for the pencil hardness (Fig. 4a) test, where E_3wt achieves 5H at 90 s, dropping to 4H at 120 s. Therefore, an exposure time of 90 s was identified as the practical upper limit for curing this epoxy system.

Using this curing window, the influence of PI concentration becomes clear (Fig. 4a). At only 1 wt% PI, hardness increases from 61 MPa at 30 s to about 215 MPa at 90 s, but the values never reach those obtained with 3 wt% PI. This behavior reflects insufficient cation generation to ensure complete epoxy conversion within short exposure times, resulting in a partially cured, mechanically weaker surface. In contrast, the 5 wt% formulation achieves the same hardness as the 3 wt% formulation at 60 s. It reaches its maximum hardness of approximately 278 MPa by 90 s, confirming that a higher initiator concentration accelerates polymerization and yields a denser, more robust network. Pencil hardness measurements follow the same trends, with the most significant increase occurring in the first minute of curing, achieving a maximum value of 6H for 5 wt% of PI, and then stabilizing once the network becomes densely cross-linked. It is observed that with 1 wt% PI, the pencil hardness achieves a similar value of 5H as 3 wt% PI, indicating that the surface-level cure is similar for these systems. Together, these results show that while 1 wt% PI cannot achieve complete in-depth conversion, concentrations of 3–5 wt% enable rapid, high-quality curing within ≤90 s, which aligns with the objective of fast UV processing. Although effective, increasing the content of cationic PI must be approached with care. Higher PI loadings may introduce several potential drawbacks relevant to industrial implementation. This includes increased material cost and the generation of larger amounts of strong acidic species that may persist in the cured network. Such residual acidity has been reported to influence long-term aging behavior and may raise concerns regarding substrate compatibility, particularly for metallic substrates where corrosion or interfacial degradation can occur [61,62]. On the other hand, the investigated system is a single-component formulation that does not require a separate curing agent. This simplifies handling, storage, and processing, and represents a practical advantage over conventional two-component epoxy coating systems. While these aspects were beyond the scope of the present study, they are important considerations for durability-critical applications and should be carefully evaluated.

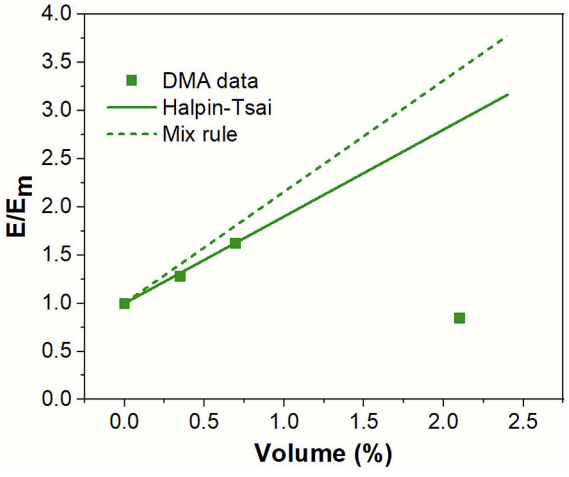

Fig. 3. Relative elastic modulus of nanocomposites (DMA data for E'_g at 25 °C in Table 2) versus NC volume fraction, fitted by the rule of mixtures (dotted line) and the Halpin-Tsai model (solid line).

When acrylate monomers are introduced to form IPNs (Fig. 4b), the hardness evolution shifts in a non-linear way. At a low acrylate content (10 wt%), both HV and pencil hardness reach their highest values, ~335 MPa and 7H, indicating an optimally densified interpenetrating network where acrylate segments reinforce the epoxy matrix [63]. Above this threshold, hardness gradually declines. Excess acrylate likely introduces phase heterogeneity or partial plasticization, diminishing network uniformity and allowing local motion that reduces surface stiffness [63,64]. This behavior reflects the typical balance observed in highly crosslinked systems, where reinforcement dominates at moderate loadings, but excessive incorporation disrupts the network architecture and lowers mechanical integrity [65].

A similar pattern appears when NC is incorporated into the IPN matrix (Fig. 4c). The HV data showed a similar linear increase (R^2 = 0.96) in hardness values up to 1 wt% NC content, in agreement with the trend observed for the DMA storage modulus at 25 °C (Table 1). Moreover, Fig. S10 demonstrates a linear correlation between storage modulus and HV values. This tendency suggests that both localized resistance to deformation and small-strain stiffness are governed by the same underlying structural factors: effective nanoclay reinforcement and network stiffening. At lower loadings (≤1 wt%), hardness increases sharply, with HV reaching ~413 MPa and pencil hardness achieving the maximum 9H rating. Well-dispersed NC platelets act as effective reinforcement sites, improving stress transfer and locally increasing crosslink density through restricted chain mobility [66]. However, once the NC concentration exceeds this optimal range, hardness decreases rapidly, following the same tendency seen in DMA. Agglomeration and poor interfacial adhesion create microstructural defects that prevent efficient stress distribution and reduce the coating's effective stiffness [67]. This mirrors the behavior seen with excessive acrylate content or insufficient PI, demonstrating that mechanical performance improves only while the network remains uniform and begins to degrade once heterogeneity becomes dominant.

To complement the experimental hardness measurements, finite element analysis (FEA) was additionally employed to estimate

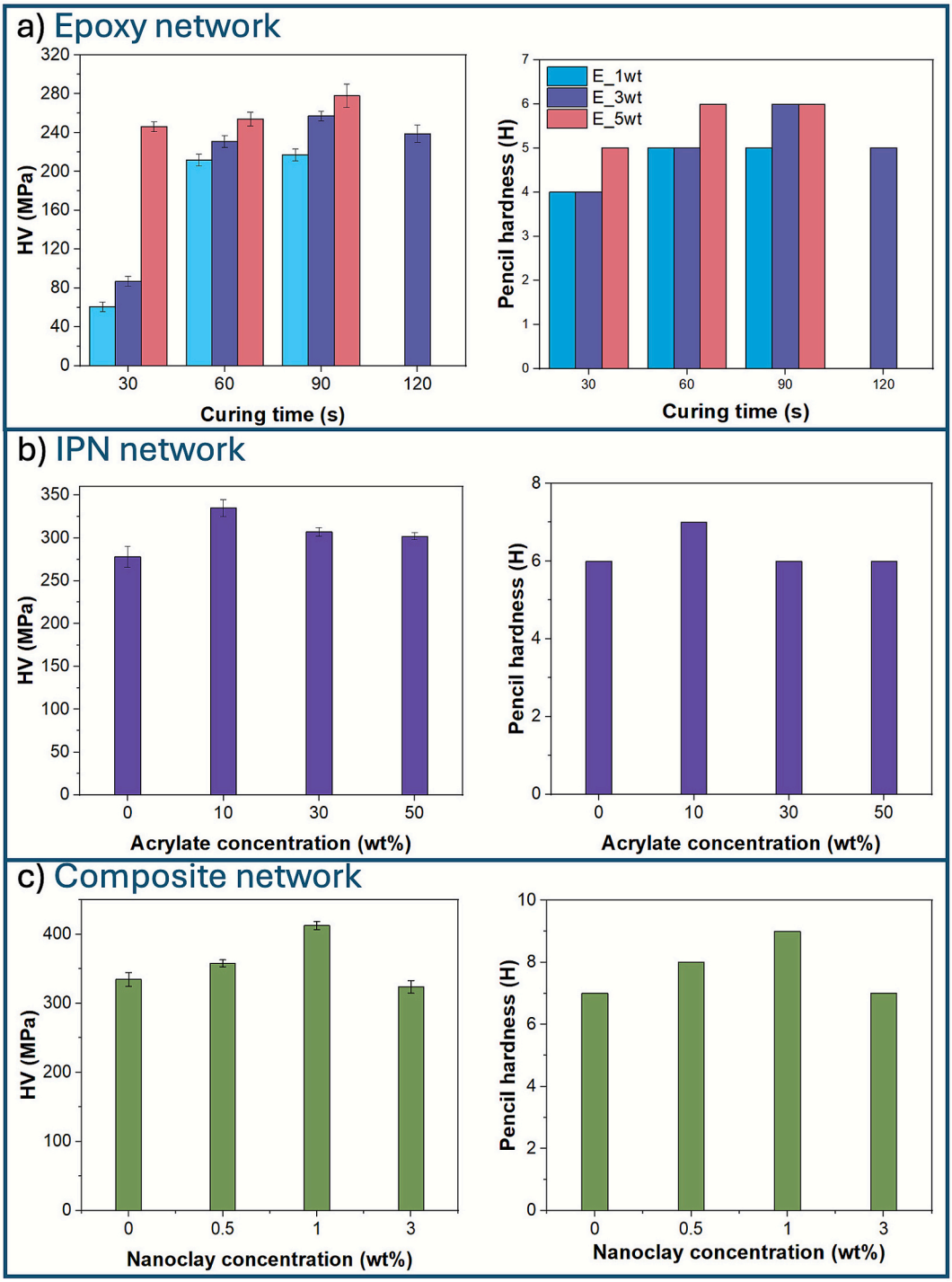

Fig. 4. Microindentation (left) and Pencil hardness (right) results for (a) samples with different curing times and PI loadings; (b) epoxy-acrylate IPN samples with different acrylate loadings, cured for 90 s; (c) IPN composites with different NC loadings.

mechanical properties such as Young's modulus and yield strength, which cannot be accurately measured directly in thin epoxy films due to their inherent brittleness [68]. By combining experimental hardness data with numerical modelling, the material parameters of the optimized formulations could be extracted reliably, further supporting the observed curing trends for IPN NC composites. Further extended details on FEA are presented in the supplementary materials (Fig. S11 and Tables S3 and S4). The FE modelling accurately reproduced the indentation process, with the simulated loading and unloading curves closely matching experimental observations [69]. The mesh was refined in the contact region between the indenter and the specimen to enhance the accuracy of the numerical simulation. Fig. 5a shows the 3D quarter-symmetry FE model geometry used for the Vickers indentation simulation; Fig. 5b presents the simulated loading step, where the indenter penetrates the polymer surface; Fig. 5c reviews the indentation area caused by the action of the indenter.

Fig. 5d illustrates the typical load-displacement curves obtained for materials with varying NC loadings. All curves exhibit the nonlinear profile characteristic of elastic-plastic deformation. The unloading segments indicate partial elastic recovery, confirming the accuracy of the

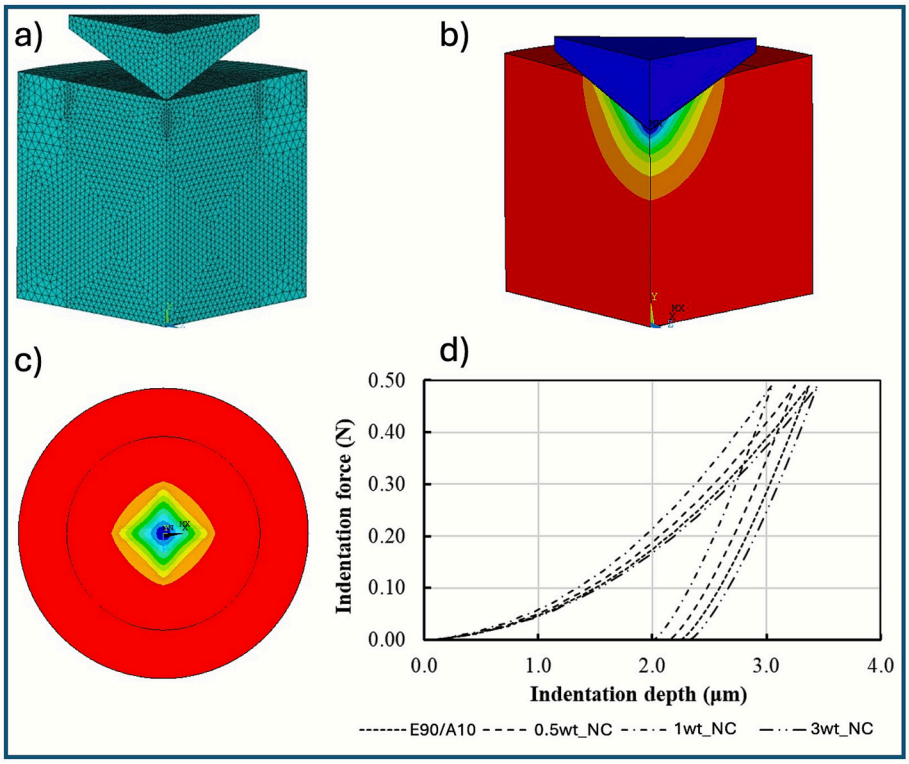

Fig. 5. (a) 3D Quarter-symmetry finite element model, (b) Distribution of displacement, (c) Simulated displacement contour, and (d) Load-displacement curve for identified parameters.

numerical model [69]. As NC content increased from 0 wt% to 1.0 wt%, the curves shifted leftward, showing smaller indentation depths at constant load (0.49 N). This behavior reflects the reinforcing effect of well-dispersed NC platelets, which hinder the motion of polymer chains and improve the matrix stiffness. At 3.0 wt%, the curves shifted to the right, corresponding to increased indentation depth and reduced hardness, likely due to nanoclay agglomeration and poorer filler dispersion, which limit stress transfer and decrease the polymerization degree, resulting from the UV-blocking effect of the filler. Overall, the experimental and simulated results demonstrate that the optimal NC concentration is approximately 1.0 wt%, at which the composite exhibits maximum hardness and yield strength. Higher nanoclay loadings promote particle clustering, incomplete cure, and degrade mechanical performance.

3.4. Water interaction and diffusion analysis

Moisture resistance is a critical parameter for the long-term performance of epoxy-based coatings, as water penetration can plasticize the network, accelerate degradation, and compromise mechanical integrity [70]. Surface wettability and bulk sorption behavior, therefore, provide valuable insight into the barrier properties considering structural uniformity of the developed IPN and nanocomposite systems. As shown in Fig. S12, both IPN formation and NC incorporation increase the water contact angle (CA) of the UV-cured coatings. The neat epoxy exhibits a CA of ~72°, which increases to ~75° upon introduction of the hydrophobic acrylate component. Addition of NC further enhances surface hydrophobicity, yielding CA values of 83–86° for the 0.5 and 1 wt% NC formulations.

Water uptake by epoxy-acrylate IPNs with varying NC loadings is presented in Fig. 6. A one-dimensional (1D) Fickian through-thickness diffusion model was considered (Eq.(8)), while diffusion along the length and width, as well as non-Fickian mechanisms, were neglected [71]. Model fitting showed satisfactory agreement with the experimental data, with R^2 values ranging from 0.80 to 0.90, considering the small specimen mass relative to the absorbed water, which increases measurement sensitivity. Nevertheless, the overall trend of water uptake is clear and consistent across all sample groups. In all systems, the weight gain increases linearly with the square root of time at the early stage of absorption, followed by saturation at the later stage. Some deviations from ideal Fickian behavior are observed in the intermediate stage, most notably for the 3 wt% NC sample (Fig. 6b). However, this aspect is beyond the scope of the present study and is therefore not discussed further.

The water saturation levels and diffusion coefficients of the materials are summarized in Table 3, showing a clear trend for the 0.5 wt% NC and 1 wt% NC nanocomposites: the water saturation level (M_∞) decreases from 7.5% to 5.3%, while the diffusion coefficient (D) decreases from $0.6 \cdot 10^{-3}$ to $0.35 \cdot 10^{-3}$ mm^2/h. This behavior is expected, as the 2D-structured NC nanoparticles incorporated into the epoxy network act as effective barriers, hindering the diffusion of water molecules through the material thickness [39].

The Nielsen model (Eq. (9)) was applied to describe the diffusivity of composites containing 2D inclusions oriented perpendicular to the direction of water ingress [72]. Schematics in Fig. 6d show how NC platelets introduce a tortuous water diffusion pathway, effectively increasing the transport resistance. The experimentally derived diffusion coefficients (Fig. 6d) show excellent agreement with the Nielsen model, except for the 3 wt% NC sample. As seen from Figs. 6(c) and 6 (d) and the data in Table 3, the 3 wt% NC sample deviates from the general behavior observed for nanocomposites with lower NC contents, due to incomplete curing and thus easier water diffusion through the low-density network. These results are in good agreement with the previously discussed DMA and microhardness data.

4. Conclusions

This study establishes a rapid and tunable sustainable route for

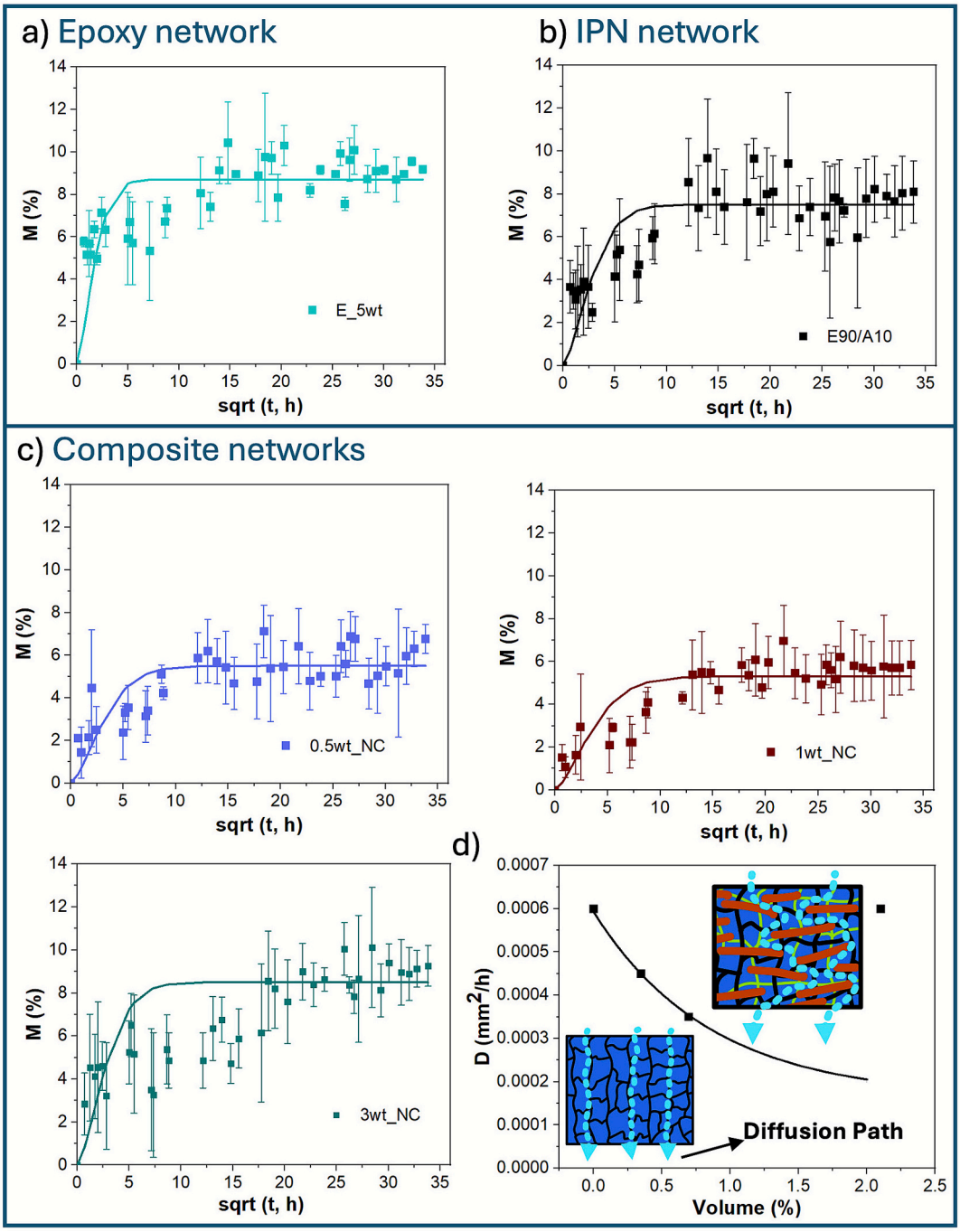

Fig. 6. Water uptake of (a) epoxy, (b) epoxy-acrylate IPNs, and (c) IPN composites with different NC loadings. Symbols represent experimental data; solid lines are fittings by Fick's model Eq. (8). (d) Schematic image of NC influenced tortuous water diffusion paths, and apparent diffusion coefficient of the nanocomposites as a function of NC volume fraction. The solid line represents the approximation using the Nielsen model (Eq. (9)).

Table 3
Diffusion characteristics of the materials.

Sample	M_∞, %	D, 10^{-3} mm^2/h
E_5wt	8.7	1.5
E90/A10	7.5	0.6
0.5wt_NC	5.5	0.45
1wt_NC	5.3	0.35
3wt_NC	8.5	0.6

producing high-performance UV-curable epoxy-acrylate coatings by systematically progressing from neat epoxy to IPNs and finally to nanoclay-reinforced IPN composites. All resin formulations cured into fully crosslinked ~300 μm films in under 2 min, eliminating the need for thermal post-processing.

IPN formation increased hardness, stiffness, and water-barrier properties, while the addition of 0.5–1 wt% nanoclay provided further reinforcement through restricted segmental mobility and enhanced network densification. Despite a modest decrease in tan δ-based apparent T_g, the storage-modulus transitions shifted to slightly higher temperatures, confirming the presence of stiffened interphase regions that govern the mechanical response. Fickian sorption modelling revealed reduced water uptake in the optimized systems, demonstrating a clear correlation between network architecture and barrier

performance. Strong agreement between indentation experiments and FEA simulations validated the hybrid experimental-computational framework as an efficient and accurate method for evaluating the mechanical behavior of thin UV-cured nanocomposite coatings.

Together, these results demonstrate a fast-curing, mechanically robust, and water-resistant coating platform that integrates photopolymerization kinetics, nanocomposite reinforcement, and predictive modelling, advancing next-generation protective materials for demanding, high-resilience applications, for example, corrosion-resistant coatings in maritime environments.

Together, these results demonstrate a fast-curing, mechanically robust, and water-resistant UV-curable coating platform. Developed approach integrates controlled photopolymerization kinetics, nanocomposite reinforcement, and predictive modelling, to advance next-generation protective materials. Still, while the present study establishes the structure-property relationships and performance potential of the system, further evaluation of environmental durability and long-term aging will be required to validate its applicability in demanding service conditions, such as corrosion-protective coatings for maritime environments.

CRediT authorship contribution statement

Maksims Jurinovs: Writing – review & editing, Writing – original draft, Visualization, Validation, Methodology, Investigation, Formal analysis, Data curation, Conceptualization. **Nikolass Rukavisnikovs:** Writing – original draft, Visualization, Investigation, Formal analysis. **Sabine Greivule:** Writing – original draft, Formal analysis. **Olesja Starkova:** Writing – review & editing, Validation, Investigation, Formal analysis. **Andrejs Kovalovs:** Writing – original draft, Validation, Software, Investigation, Formal analysis. **Jānis Brunāvs:** Writing – review & editing. **Jan Macutkevič:** Writing – review & editing. **Inna Juhnevica:** Investigation, Formal analysis. **Oskars Platnieks:** Writing – review & editing, Investigation, Formal analysis. **Sergejs Gaidukovs:** Writing – review & editing, Supervision, Resources, Project administration, Methodology, Funding acquisition, Conceptualization.

Declaration of competing interest

The authors declare that they have no known competing financial interests or personal relationships that could have appeared to influence the work reported in this paper.

Acknowledgments

This work was supported by grant No RTU-IG-2024/1-0010 under the EU Recovery and Resilience Facility funded project No. 5.2.1.1.i.0/2/24/I/CFLA/003 “Implementation of consolidation and management changes at Riga Technical University, Liepaja University, Rezekne Academy of Technology, Latvian Maritime Academy and Liepaja Maritime College for the progress towards excellence in higher education, science, and innovation”.

Appendix A. Supplementary data

Supplementary data to this article can be found online at https://doi.org/10.1016/j.reactfunctpolym.2026.106664.

Data availability

Data will be made available on request.

References

[1] S.B. Lyon, R. Bingham, D.J. Mills, Advances in corrosion protection by organic coatings: what we know and what we would like to know, Prog. Org. Coat. 102 (2017) 2–7.
[2] I.P. Okokpujie, L.K. Tartibu, H.O. Musa-Basheer, A.O.M. Adeoye, Effect of coatings on mechanical, corrosion and tribological properties of industrial materials: a comprehensive review, J. Bio- and Tribo-Corros. 10 (1) (2023) 2.
[3] D. Duraccio, P.P. Capra, G. Malucelli, UV-curable coatings for energy harvesting applications: current state-of-the-art and future perspectives, Micro Nano Eng. 23 (2024) 100266.
[4] S. Anwar, X. Li, A review of high-quality epoxy resins for corrosion-resistant applications, J. Coat. Technol. Res. 21 (2) (2024) 461–480.
[5] A. Makinde, B. Makinde-Isola, I. Oladele, A. Akinwekomi, D.O. Bichang’a, applications of epoxy resin: adhesives, coatings, and composites, in: P. Vizureanu, M.S. Bălţatu (Eds.), Epoxy – Materials, Applications and Advanced Technologies, IntechOpen, London, 2025.
[6] D. Aoki, S. Dogoshi, Y. Ito, K. Arimitsu, Thermal curing of epoxy resins at lower temperature using 4-(methylamino)pyridine derivatives as novel thermal latent curing agents, J. Polym. Sci. 62 (19) (2024) 4406–4415.
[7] H. Sreehari, V. Gopika, J.S. Jayan, A.S. Sethulekshmi, A. Saritha, A comprehensive review on bio epoxy based IPN: synthesis, properties and applications, Polymer 252 (2022) 124950.
[8] C. Mendes-Felipe, J. Oliveira, I. Etxebarria, J.L. Vilas-Vilela, S. Lanceros-Mendez, State-of-the-art and future challenges of UV curable polymer-based smart materials for printing technologies, Adv. Mater. Technol. 4 (3) (2019) 1800618.
[9] D. Czachor-Jadacka, B. Pilch-Pitera, Progress in development of UV curable powder coatings, Prog. Org. Coat. 158 (2021) 106355.
[10] X. He, L. Zang, Y. Xin, Y. Zou, An overview of photopolymerization and its diverse applications, Appl. Theatr. Res. 2 (6) (2023) e202300030.
[11] C. Decker, The use of UV irradiation in polymerization, Polym. Int. 45 (2) (1998) 133–141.
[12] Y. Chen, R. Liu, J. Luo, Enhancing weathering resistance of UV-curable coatings by using TiO2 particles as filler, Prog. Org. Coat. 169 (2022) 106936.
[13] P. Bednarczyk, K. Walkowiak, I. Irska, Epoxy (meth)acrylate-based thermally and UV initiated curable coating systems, Polymers 15 (24) (2023) 4664.
[14] A. Barkane, O. Platnieks, J. Vecstaudza, S. Gaidukovs, Analysis of bio-based acrylate accelerated weathering: a study of nanocellulose impact on the bulk durability of 3D-printed nanocomposites, Mater. Today Chem. 33 (2023) 101737.
[15] A. Kausar, Interpenetrating polymer network and nanocomposite IPN of polyurethane/epoxy: a review on fundamentals and advancements, Polym.-Plast. Technol. Mater. 58 (7) (2019) 691–706.
[16] J.R. Nowers, B. Narasimhan, The effect of interpenetrating polymer network formation on polymerization kinetics in an epoxy-acrylate system, Polymer 47 (4) (2006) 1108–1118.
[17] Y. Ma, Z. Liu, P. Li, M. Li, Y. Zhao, Fabrication of epoxy resin/acrylate IPNs magnetorheological material with oil-surface bonding for damage repair of long-distance oil pipelines, Cem. Concr. Compos. 131 (2022) 104572.
[18] X. Fan, X. Wang, H. Yan, M. Cai, W. Zhong, H. Li, M. Zhu, Interpenetrating network polymer (IPN) composite coating containing fluorinated polyacrylic complex latex particles toward high wear and corrosion resistance, Colloids Surf. A Physicochem. Eng. Asp. 639 (2022) 128323.
[19] A. Idris, A. Muntean, B. Mesic, A review on predictive tortuosity models for composite films in gas barrier applications, J. Coat. Technol. Res. 19 (3) (2022) 699–716.
[20] R.V. Sankaranarayanan, S.H. Menon, S.C. Maniyeri, V.K. Periya, S. Naveenchandra Prabhu, A comprehensive review on gas barrier polymer nanocomposites: materials, characterization, synthesis, applications, and modelling approaches, ChemistrySelect 10 (41) (2025) e04165.
[21] J. George, B. Aaliya, K.V. Sunooj, R. Kumar, An overview of higher barrier packaging using nanoadditives, Nanotechnol. Enhanced Food Packag. (2022) 235–264.
[22] N. Affaf, J. Alias, N. Alang, Montmorillonite (MMT) nanoclay in smart coatings for corrosion protection of metal alloy: a brief review, J. Phys. Conf. Ser. 2688 (1) (2024) 012012.
[23] Y. Wang, Z. Cao, F. Liu, X. Xue, Synthesis and characterization of UV-curing epoxy acrylate coatings modified with organically modified rectorite, J. Coat. Technol. Res. 14 (1) (2017) 107–115.
[24] M. Turna, F. Şen, S. Madakbaş, S. Karataş, Preparation and characterization of UV-cured epoxy acrylate-based nanocomposite coatings containing organonanoclay, Polym. Bull. 80 (7) (2023) 7949–7969.
[25] C. Noè, L. Iannucci, S. Malburet, A. Graillot, S. Grassini, Vanillin-based photocurable anticorrosion coatings reinforced with Nanoclays, Macromol. Mater. Eng. 309 (11) (2024) 2400155.
[26] M.N. Uddin, M.T. Hossain, N. Mahmud, S. Alam, M. Jobaer, S.I. Mahedi, A. Ali, Research and applications of nanoclays: a review, SPE Polym. 5 (4) (2024) 507–535.
[27] F.M. Uhl, B.R. Hinderliter, S.P. Davuluri, S.G. Croll, S.-C. Wong, D.C. Webster, UV curable polymers with organically modified clay as the Nanoreinforcements, MRS Online Proc. Libr. 788 (1) (2004) 1145.
[28] A. Rigail-Cedeño, D.F. Schmidt, Bio-based epoxy clay nanocomposites, AIP Conf. Proc. 1914 (1) (2017) 030023.
[29] M. Sangermano, W. Carbonaro, G. Malucelli, A. Priola, UV-cured interpenetrating acrylic-epoxy polymer networks: preparation and characterization, Macromol. Mater. Eng. 293 (6) (2008) 515–520.

[30] U. Farooq, J. Teuwen, C. Dransfeld, Toughening of epoxy systems with interpenetrating polymer network (IPN): a review, Polymers (2020) 1908.
[31] C. Decker, L. Keller, K. Zahouily, S. Benfarhi, Synthesis of nanocomposite polymers by UV-radiation curing, Polymer 46 (17) (2005) 6640–6648.
[32] M. Shettar, C.S.S. Kowshik, M. Manjunath, P. Hiremath, Experimental investigation on mechanical and wear properties of nanoclay–epoxy composites, J. Mater. Res. Technol. 9 (4) (2020) 9108–9116.
[33] S. Gaidukovs, A. Medvids, P. Onufrijevs, L. Grase, UV-light-induced curing of branched epoxy novolac resin for coatings, Express Polym Lett 12 (10) (2018) 918–929.
[34] Z.-S. Guo, J. Feng, H. Wang, H. Hu, J. Zhang, A new temperature-dependent modulus model of glass/epoxy composite at elevated temperatures, J. Compos. Mater. 47 (26) (2012) 3303–3310.
[35] R.D. Maksimov, S. Gaidukovs, M. Kalnins, J. Zicans, E. Plume, A nanocomposite based on a styrene-acrylate copolymer and native montmorillonite clay 2. Modeling the elastic properties, Mech. Compos. Mater. 42 (2) (2006) 163–172.
[36] R.D. Maksimov, A. Lagzdins, N. Lilichenko, E. Plume, Mechanical properties and water vapor permeability of starch/montmorillonite nanocomposites, Polym. Eng. Sci. 49 (12) (2009) 2421–2429.
[37] D.A. Brune, J. Bicerano, Micromechanics of nanocomposites: comparison of tensile and compressive elastic moduli, and prediction of effects of incomplete exfoliation and imperfect alignment on modulus, Polymer 43 (2) (2002) 369–387.
[38] O. Starkova, O. Platnieks, A. Sabalina, S. Gaidukovs, Hydrothermal ageing effect on reinforcement efficiency of nanofibrillated cellulose/biobased poly(butylene succinate) Composites, Polymers 14 (2) (2022) 221.
[39] T. Glaskova, A. Aniskevich, Moisture absorption by epoxy/montmorillonite nanocomposite, Compos. Sci. Technol. 69 (15) (2009) 2711–2715.
[40] S. Zid, M. Zinet, E. Espuche, Modeling diffusion mass transport in multiphase polymer systems for gas barrier applications: a review, J. Polym. Sci. B Polym. Phys. 56 (8) (2018) 621–639.
[41] C. Decker, K. Moussa, Kinetic study of the cationic photopolymerization of epoxy monomers, J. Polym. Sci. Part A Polym. Chem. 28 (12) (1990) 3429–3443.
[42] B. Golaz, V. Michaud, Y. Leterrier, J.A.E. Månson, UV intensity, temperature and dark-curing effects in cationic photo-polymerization of a cycloaliphatic epoxy resin, Polymer 53 (10) (2012) 2038–2048.
[43] J.F. Rabek, Polymer Photodegradation, 1st ed., Springer Dordrecht, 2012.
[44] T.J. Horr, J. Ralston, R.S.C. Smart, FT-IR diffuse reflectance study of the adsorption and oxidation of alcohols on porous silica surfaces, Colloids Surf., A 63 (1) (1992) 21–28.
[45] R. Acosta Ortiz, A.E. García Valdez, D. Hernández Cruz, G. Nestoso Jiménez, A. I. Hernández Jiménez, J.G. Téllez Padilla, R. Guerrero Santos, Highly reactive novel biobased cycloaliphatic epoxy resins derived from nopol and a study of their cationic photopolymerization, J. Polym. Res. 27 (6) (2020) 144.
[46] R.S.C. Woo, Y. Chen, H. Zhu, J. Li, J.-K. Kim, C.K.Y. Leung, Environmental degradation of epoxy–organoclay nanocomposites due to UV exposure. Part I: photo-degradation, Compos. Sci. Technol. 67 (15) (2007) 3448–3456.
[47] J. Baselga, M. González, J.C. Cabanelas, Applications of FTIR on epoxy resins - identification, monitoring the curing process, phase separation and water uptake, in: T. Theophanides (Ed.), Infrared Spectroscopy - Materials Science, Engineering and Technology, IntechOpen, London, 2012.
[48] C. Esposito Corcione, M. Frigione, A. Maffezzoli, G. Malucelli, Photo – DSC and real time – FT-IR kinetic study of a UV curable epoxy resin containing o-Boehmites, Eur. Polym. J. 44 (7) (2008) 2010–2023.
[49] F.M. Uhl, D.C. Webster, S.P. Davuluri, S.-C. Wong, UV curable epoxy acrylate–clay nanocomposites, Eur. Polym. J. 42 (10) (2006) 2596–2605.
[50] H. Datta, N.K. Singha, A.K. Bhowmick, Beneficial effect of Nanoclay in atom transfer radical polymerization of ethyl acrylate: a one pot preparation of tailor-made polymer nanocomposite, Macromolecules 41 (1) (2008) 50–57.
[51] R. Peila, G. Malucelli, A. Priola, Preparation and characterization of UV-cured acrylic nanocomposites based on modified organophilic montmorillonites, J. Therm. Anal. Calorim. 97 (3) (2009) 839–844.
[52] K. Muralishwara, Y.N. Sudhakar, U.A. Kini, S. Sharma, B.M. Gurumurthy, Moisture absorption and spectroscopic studies of epoxy clay nanocomposite, Polym. Bull. 79 (7) (2022) 5587–5611.
[53] T.A. Nguyen, T.M.H. Pham, Study on the properties of epoxy composites using fly ash as an additive in the presence of nanoclay: mechanical properties, flame retardants, and dielectric properties, J. Chemother. 2020 (1) (2020) 8854515.
[54] T.-Y. Tsai, N. Bunekar, C.-C. Huang, Y.-S. Huang, L.-C. Chen, Novolac cured epoxy resin/fullerene modified clay composites: applied to copper clad laminates, RSC Adv. 5 (116) (2015) 95649–95656.
[55] R. Mahmudzade, P. Nikaeen, W. Chirdon, A. Khattab, D. Depan, Photodegradation mechanisms and physico-chemical properties of EPON-IPD epoxy-based polymers, React. Funct. Polym. 178 (2022) 105351.
[56] A. Barkane, O. Platnieks, M. Jurinovs, S. Gaidukovs, Thermal stability of UV-cured vegetable oil epoxidized acrylate-based polymer system for 3D printing application, Polym. Degrad. Stab. 181 (2020) 109347.
[57] S. Im, K. Kim, M. Yun, T.-Y. Cho, J.-H. Eom, S.-K. Cho, Cross-link density and moisture barrier properties of organic films prepared by the dual curing of epoxy–acrylate hybrid networks in various solvents, Prog. Org. Coat. 191 (2024) 108443.
[58] J. Casado, O. Konuray, A. Roig, X. Fernández-Francos, X. Ramis, 3D printable hybrid acrylate-epoxy dynamic networks, Eur. Polym. J. 173 (2022) 111256.
[59] R.D. Maksimov, S. Gaidukovs, J. Zicans, M. Kalnins, E. Plume, V. Spacek, P. Sviglerova, Nanocomposites based on a styrene-acrylate copolymer and organically modified montmorillonite 1. Mechanical properties, Mech. Compos. Mater. 42 (3) (2006) 263–272.
[60] A. Visvanathan, N. Ilie, R. Hickel, K.-H. Kunzelmann, The influence of curing times and light curing methods on the polymerization shrinkage stress of a shrinkage-optimized composite with hybrid-type prepolymer fillers, Dent. Mater. 23 (7) (2007) 777–784.
[61] L. Yang, J. Yang, J. Nie, X. Zhu, Temperature controlled cationic photo-curing of a thick, dark composite, RSC Adv. 7 (7) (2017) 4046–4053.
[62] W.L. Koay, E. Ye, C.-L.K. Lee, X.J. Loh, Y. Lu, V.X. Truong, Red light activatable photobase generator for rapid thiol-nucleophilic polymerization, Mater. Today Chem. 35 (2024) 101872.
[63] I. Calvez, C.R. Szczepanski, V. Landry, Hybrid free-radical/cationic phase-separated UV-curable system: impact of Photoinitiator content and monomer fraction on surface morphologies and gloss appearance, Macromolecules 55 (8) (2022) 3129–3139.
[64] B.T. Hong, K.S. Shin, D.S. Kim, Ultraviolet-curing behavior of an epoxy acrylate resin system, J. Appl. Polym. Sci. 98 (3) (2005) 1180–1185.
[65] D.K. Chattopadhyay, S.S. Panda, K.V.S.N. Raju, Thermal and mechanical properties of epoxy acrylate/methacrylates UV cured coatings, Prog. Org. Coat. 54 (1) (2005) 10–19.
[66] C.-K. Lam, K.-T. Lau, Optimization effect of Micro hardness by nanoclay clusters in nanoclay/epoxy composites, J. Thermoplast. Compos. Mater. 22 (2) (2009) 213–225.
[67] K. Muralishwara, U.A. Kini, S. Sharma, Surface properties of epoxy clay nanocomposite coating, Mater. Today Proc. 38 (2021) 2725–2731.
[68] R. Voo, M. Mariatti, L.C. Sim, Flexibility improvement of epoxy nanocomposites thin films using various flexibilizing additives, Compos. Part B Eng. 43 (8) (2012) 3037–3043.
[69] A. Kovalovs, A. Chate, S. Gaidukovs, A. Medvids, Finite Element Simulation of Indentation Experiment on Branched Epoxy Novolac Resin, 2019.
[70] K. Sabet-Bokati, K. Plucknett, Water-induced failure in polymer coatings: mechanisms, impacts and mitigation strategies—a comprehensive review, Polym. Degrad. Stab. 230 (2024) 111058.
[71] R.D. Maksimov, S. Gaidukov, J. Zicans, J. Jansons, Moisture permeability of a polymer nanocomposite containing unmodified clay, Mech. Compos. Mater. 44 (5) (2008) 505–514.
[72] R.D. Maksimov, S. Gaidukovs, J. Zicans, M. Kalnins, E. Plume, V. Spacek, P. Sviglerova, A nanocomposite based on a styrene-acrylate copolymer and organically modified montmorillonite 2. Barrier and thermal properties, Mech. Compos. Mater. 42 (4) (2006) 353–362.